

Three-dimensional imaging of the unsectioned adult spinal cord to assess axon regeneration and glial responses after injury

Ali Ertürk^{1,2}, Christoph P Mauch³, Farida Hellal^{1,4}, Friedrich Förstner⁵, Tara Keck^{6,7}, Klaus Becker^{8,9}, Nina Jähring⁸⁻¹⁰, Heinz Steffens¹¹, Melanie Richter¹², Mark Hübener⁶, Edgar Kramer¹², Frank Kirchhoff^{11,13}, Hans Ulrich Dodt^{8,9} & Frank Bradke^{1,4}

Studying regeneration in the central nervous system (CNS) is hampered by current histological and imaging techniques because they provide only partial information about axonal and glial reactions. Here we developed a tetrahydrofuran-based clearing procedure that renders fixed and unsectioned adult CNS tissue transparent and fully penetrable for optical imaging. In large spinal cord segments, we imaged fluorescently labeled cells by 'ultramicroscopy' and two-photon microscopy without the need for histological sectioning. We found that more than a year after injury growth-competent axons regenerated abundantly through the injury site. A few growth-incompetent axons could also regenerate when they bypassed the lesion. Moreover, we accurately determined quantitative changes of glial cells after spinal cord injury. Thus, clearing CNS tissue enables an unambiguous evaluation of axon regeneration and glial reactions. Our clearing procedure also renders other organs transparent, which makes this approach useful for a large number of preclinical paradigms.

Diverse disease studies, ranging from tumor pathology to neurodegeneration, rely on histological sectioning. However, in many cases, this approach yields incomplete spatial information and is, therefore, prone to misinterpretation. In particular, there are varying reports about the effectiveness of experimental interventions that produce axonal regeneration in the injured adult CNS¹⁻⁶. One major reason for the discrepancies is that tissue sections provide a two-dimensional picture of the regenerating axons, showing only fragments. Hence, it is often unclear where the candidate regenerating axon derives from and where it ends⁶. Thereby, spared axons can be mistaken for regenerating axons in histological sections. Similarly, whereas the response of glial cells to spinal cord injury is a key pathological event⁷, existing

methods are largely restricted to tissue sectioning and subsequent extrapolation of the total glial population⁸⁻¹⁰.

To unequivocally trace axonal trajectories and evaluate regenerating axons, it would be ideal to image axons in unsectioned CNS tissue⁶. So far, however, it is not possible to visualize samples as thick as the rodent spinal cord at microscopic resolution because light is scattered in such tissue. This restricts current imaging techniques, including two-photon imaging¹¹, to superficially coursing axons¹¹⁻¹³.

One potential way to overcome this obstacle is tissue clearing¹⁴. In the clearing procedure, the tissue is dehydrated and subsequently immersed in a solution that has the refractive index of proteins; thereby, the tissue becomes transparent and light does not scatter. We recently applied this approach to dissected hippocampi of young mice¹⁵. However, this procedure does not allow visualization of adult tissue containing a high degree of lipids and a sturdy extracellular matrix, precluding the use of this technique for a wide range of preclinical paradigms.

To overcome these limitations, we developed a tetrahydrofuran (THF)-based clearing technique that makes the adult spinal cord and brainstem of rodents transparent and, thereby, amenable to deep tissue fluorescence imaging. Using this method, we determined the trajectories of regenerating sensory axons and found that growth-competent axons as well as axons that have been considered to be growth incompetent show regenerative features. Our results suggest that visualizing cells in unsectioned CNS tissue holds promise for assessing experimental therapies in spinal cord injury and other neurological pathologies.

RESULTS

3D imaging of neurons in adult unsectioned CNS tissue

We set out to develop a clearing technique that would render adult and myelinated CNS tissue transparent while preserving the

¹Max Planck Institute of Neurobiology, Axonal Growth and Regeneration, Martinsried, Germany. ²Department of Neuroscience, Genentech, South San Francisco, California, USA. ³Max Planck Institute of Psychiatry, Munich, Germany. ⁴Deutsches Zentrum für Neurodegenerative Erkrankungen, Axonal Growth and Regeneration, Bonn, Germany. ⁵Max Planck Institute of Neurobiology, Systems and Computational Neurobiology, Martinsried, Germany. ⁶Max Planck Institute of Neurobiology, Cellular and Systems Neurobiology, Martinsried, Germany. ⁷Medical Research Council Centre for Developmental Neurobiology, King's College London, Guy's Hospital Campus, London, UK. ⁸Technical University Vienna, Institute of Solid State Electronics, Department of Bioelectronics, Vienna, Austria. ⁹Center for Brain Research, Medical University of Vienna, Section of Bioelectronics, Vienna, Austria. ¹⁰University of Oldenburg, Department of Neurobiology, Oldenburg, Germany. ¹¹Glial Physiology and Imaging, Department of Neurogenetics, Max Planck Institute of Experimental Medicine, Göttingen, Germany. ¹²Development and Maintenance of the Nervous System, Centre for Molecular Neurobiology, Hamburg, Germany. ¹³Molecular Physiology, Institute of Physiology, University of Saarland, Homburg/Saar, Germany. Correspondence should be addressed to F.B. (frank.bradke@dzne.de).

Received 20 December 2010; accepted 26 May 2011; published online 25 December 2011; doi:10.1038/nm.2600

structural integrity of cells. To this end, we fixed spinal cords from GFP-M mice expressing GFP in a sparse neuronal population¹⁶ and screened various compounds to dehydrate and delipidate the tissue. From this screen, only THF rendered adult CNS tissue accessible to clearing, which resulted in a transparent spinal cord (Fig. 1a and Supplementary Fig. 1).

We first tested whether THF-based clearing allows imaging through the entire thickness of the spinal cord. Whereas uncleared tissue could only be imaged up to a depth of $292 \pm 48 \mu\text{m}$ ($n = 23$ spinal cords) by two-photon microscopy, cleared spinal cords could be scanned in their entire depth at high resolution ($1,355 \pm 69 \mu\text{m}$ at lumbar 1 (L1) spine level; $n = 11$ spinal cords, $**P < 0.01$, t test; Fig. 1b,c and Supplementary Video 1). Ventral axons, deep in the cleared spinal cord were imaged with a resolution similar to axons close to the dorsal surface (Fig. 1d–g). Fine protrusions were also visible in the cleared spinal cord, including axonal boutons in the gray matter (Fig. 1g,h). Clearing also substantially improved the resolution in confocal microscopy, particularly in the z dimension (Supplementary Fig. 2 and Supplementary Video 2).

To test whether axons could be followed over long distances, we imaged large-size cleared spinal cord tissue samples from GFP-M mice (Fig. 2a) by ultramicroscopy¹⁵. With this approach, the specimen is imaged from above using a large field of view and the optical plane in focus is illuminated from the side (Fig. 2b), resulting in an increased z resolution. We imaged 3- to 4-mm-long spinal cord segments (Fig. 2a,c and Supplementary Video 3) and lower parts of the brainstem (Supplementary Fig. 3 and Supplementary Video 4). Axons were visualized up to 4 mm (Fig. 2c; between thoracic 12 (T12) and L2). The fine z resolution of the images allowed optical sectioning of the tissue (Fig. 2d) that was virtually indistinguishable from histological sections. On the basis of the collected images, we traced the white and gray matter boundaries and axon bundles (Fig. 2e).

Like genetically encoded indicators, synthetic fluorophores were also preserved during the clearing procedure. We traced rat corticospinal tract axons of the hindlimb sensorimotor cortex with biotin dextran amine conjugated to rhodamine and visualized labeled corticospinal tract axons in three dimensions (3D) after clearing (Supplementary Fig. 4 and Supplementary Video 5). In addition, we could also image immunolabeled axons in the spinal cord after clearing (Supplementary Fig. 5). We conclude that THF-based clearing renders fluorescently labeled neuronal processes amenable to imaging in the unsectioned tissue through their entire depth.

3D imaging of injured and regenerating axons

We next applied this technique to axons lesioned after spinal cord injury. To visualize injured axons in the unsectioned spinal cord, we combined live imaging with subsequent clearing and 3D imaging. In GFP-M mice, we imaged the sensory axons in the dorsal column¹⁷

before and immediately after the lesion (at the level of the L1 spine) to verify transection of the axons and 5–6 h after injury to confirm retraction of the target axons (Supplementary Fig. 6a–c). At 10 d after injury, we perfused the mice and imaged the fixed lesion sites before clearing (Supplementary Fig. 6d). After clearing the tissue, we imaged the spinal cord by ultramicroscopy or two-photon microscopy and followed the projection of injured sensory axons (Supplementary Fig. 6e–j and Supplementary Videos 6 and 7). Notably, the quality of the images allowed us to unequivocally identify, segment and trace axons (Supplementary Fig. 7). Axons identified by *in vivo* imaging and postmortem fixed tissue were easily recognizable in the 3D reconstructions of the cleared spinal cord (Supplementary Fig. 6a,d,e,g). In the dorsal and deeper regions of the spinal cord, we observed sprouts that reached up to the lesion site (Supplementary Fig. 6g–j). However, most of the axons retracted and formed retraction bulbs (Supplementary Fig. 6j; $31 \pm 75 \mu\text{m}$; $n = 7$ mice).

We then assessed trajectories of regenerating axons in the injured and cleared spinal cord. Preconditioning of primary sensory neurons (that is, lesioning their peripheral axon before injuring their central axon) elicits a robust regenerative response in the CNS^{4,11}. We conditioned L4 and L5 dorsal root ganglion neurons of GFP-M mice

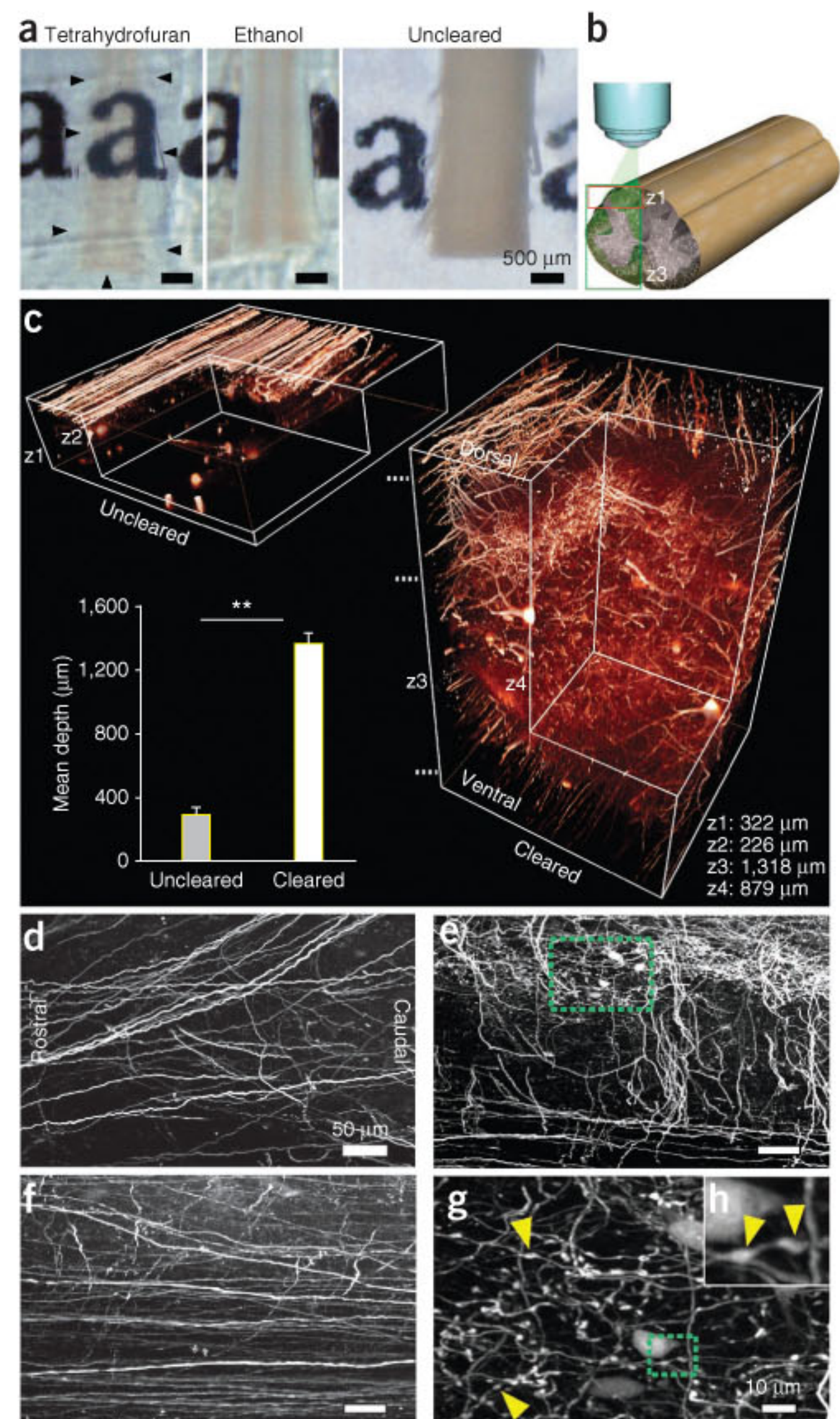
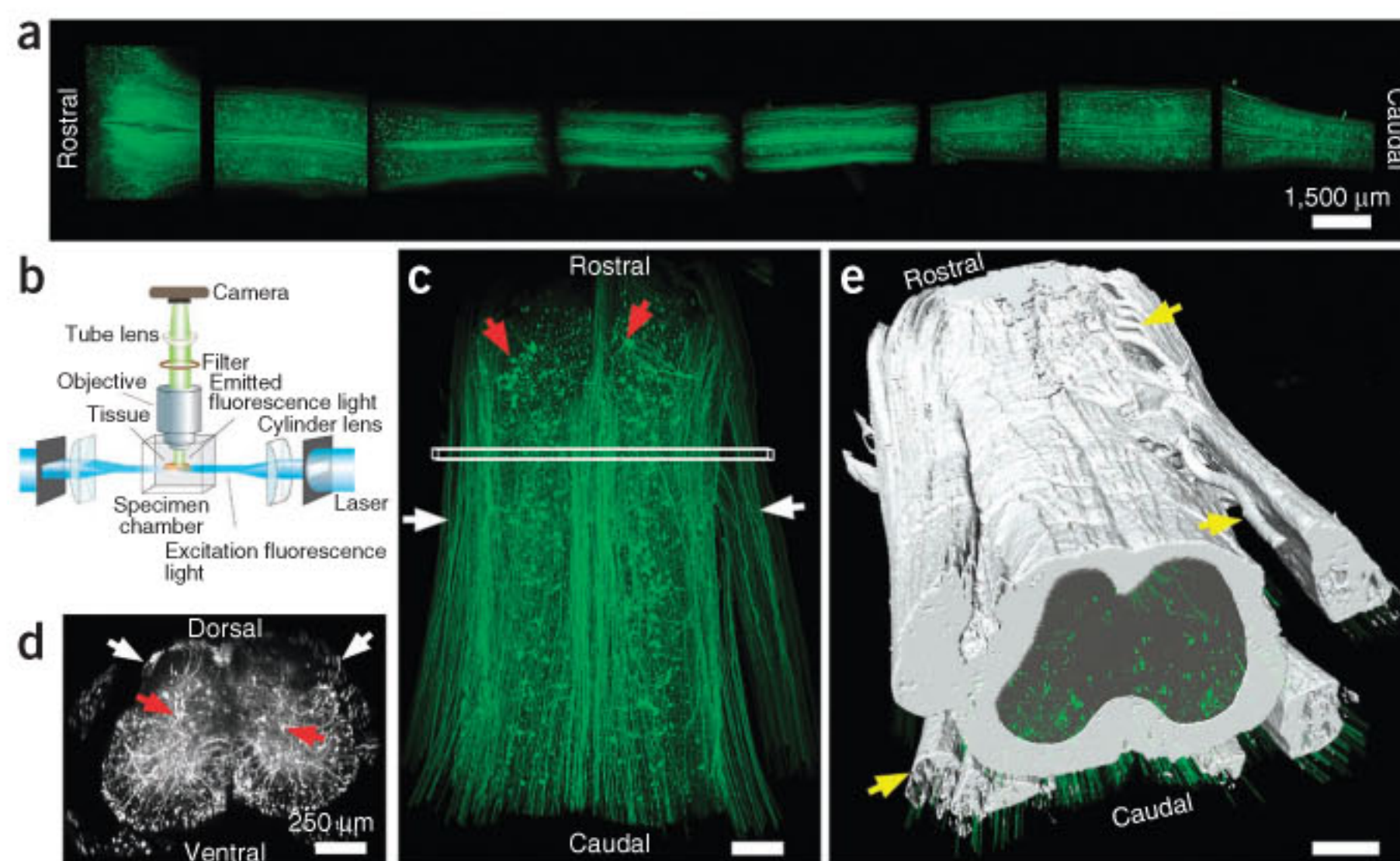


Figure 1 Clearance allows high-resolution imaging of the unsectioned spinal cord. (a) Clearance with THF renders the adult mouse spinal cord transparent (outlined by black arrowheads) while ethanol-treated tissue remains opaque (photographic images are shown). (b) Schematic illustration of the two-photon-imaged regions and depths: only dorsal (z1) or entire dorsoventral (z3) spinal cord. (c) Comparison between uncleared (left) and cleared (right) spinal cords of GFP-M mice imaged with two-photon microscopy. Values are mean \pm s.d. (d–g) Horizontal projections from the cleared spinal cord at different depths marked in c: dorsal ($\sim 100 \mu\text{m}$) (d), mid ($\sim 500 \mu\text{m}$) (e) and ventral ($\sim 1,200 \mu\text{m}$) (f). (g) Higher magnification of the area marked in green in e. (h) Higher magnification of the area marked in green in g. Yellow arrowheads in g and h depict some of the axonal boutons in the gray matter.

Figure 2 Imaging large regions of the spinal cord of GFP-M mice. (a) Entire spinal cord of a GFP-M mouse cut into 3- to 4-mm-long segments, cleared and imaged with ultramicroscopy. (b) Drawing of the ultramicroscopy setup showing tissue positioning and the light path. (c) A spinal cord segment (length 4 mm, T12 to L2 spine level) of a GFP-M mouse scanned with ultramicroscopy shown in a horizontal view. (d) Cross-view projection (50- μ m thickness) of the indicated region in c. White arrows in c,d mark individual axons in the white matter; red arrows mark cell bodies in the gray matter. (e) Traced white and gray matter boundaries and axon bundles (yellow arrows).



by cutting and ligating the sciatic nerve¹¹ 1 week before a unilateral dorsal spinal cord hemisection at the L1 level. The mice were perfused 10 d after CNS injury, and axons at the lesion site were traced back to their dorsal root ganglions to validate that they were derived from neurons whose peripheral axon had been cut¹¹. 3D visualization showed substantially more regenerating axons in deeper layers that were not visible in uncleared tissue (**Supplementary Fig. 8**). Some of these axons regenerated into and beyond the lesion site (**Fig. 3a,b**, **Supplementary Fig. 8** and **Supplementary Video 8**). We readily traced the trajectories of conditioned regenerating axons up to their tips even through deep regions of the spinal cord (**Fig. 3c,d**). Regenerating axons crossed the lesion by about 2 mm (**Fig. 3a–c,e**; $1,865 \pm 212 \mu\text{m}$; $n = 6$ mice, $**P < 0.01$, t test compared to unconditioned CNS-lesioned mice; for a complete set of two-dimensional projections see **Supplementary Fig. 9**). Notably, we found that $30.1 \pm 7.8\%$ of the conditioned sprouts deviated from their regular trajectories in the white matter and projected through various regions of the gray matter, into laminae I–VI of the spinal cord dorsal horn (**Fig. 3f,g**; $n = 24$ out of 85 axons in six mice). These axons were easily traced by 3D visualization of the unsectioned spinal cord from 1–2 mm caudal to the lesion up to 2–3 mm rostral to the lesion, that is, 4–5 mm in total length (**Fig. 3f,g**).

Studying regeneration in chronic injuries is particularly difficult, as regenerating axons course over long distances in different regions of the spinal cord. We therefore analyzed trajectories of conditioned and unconditioned axons in the same cleared spinal cords 13–18 months after spinal cord injury (**Fig. 4a–c**; $n = 4$ mice). To this end, we generated virtual nested cylindrical regions along each spinal cord hemisphere from the lesion epicenter to the periphery in 75- μ m radial increments for 3D Sholl analysis (**Fig. 4d,e**). Conditioned axons regrew directly through the injury site (**Fig. 4d**); more than 20% of the regenerating axon volume was within the inner 150- μ m region (**Fig. 4a,d,f**). These axons coursed along the caudo-rostral axis and crisscrossed in the dorsoventral and lateromedial axes. In addition, conditioned axons showed a high intersecting rate, crossing the cylindrical planes more than seven times along their regenerative path (**Fig. 4d,g** and **Supplementary Video 9**). Hence, the conditioned axons had very complex trajectories in the chronically injured spinal cord.

Live imaging has revealed that unconditioned axons can show some initial sprouts and grow during the first few days after injury^{11,12,17}. However, further regeneration of these sprouts could not be assessed by histological approaches. We observed regeneration of a few unconditioned axons in chronically injured spinal cords, albeit less extensively than conditioned axons. Most of these axons protruded the peripheral zone of the lesion showing less than 7% of the axonal

volume within the inner 150- μ m region (**Fig. 4d,f**). Moreover, along their trajectories they intersected only three times with the cylindrical planes (**Fig. 4g**). These axons were readily unveiled by 3D imaging because of their abnormal trajectories (**Supplementary Fig. 10a**) and identifiable tips (**Supplementary Fig. 11**), the key criteria for unequivocally distinguishing regenerating axons from spared axons, which course on their normal path until the edge of imaged tissue segment and show no identifiable tip (**Supplementary Fig. 10a**). By contrast, conventional histological sectioning would reveal only axon fragments (**Supplementary Fig. 10b–h**) omitting key information, including a defined axonal tip and trajectory. Hence, regenerating axons would be indistinguishable from spared axons by conventional sectioning. Thus, our data indicate that unconditioned axons not only show some initial sprouting^{11,12,17} but regenerate if they can bypass the lesion.

3D distribution of microglia and astrocytes after injury

Despite the key role of microglia and astrocytes during spinal cord injury, relatively little is known about their cell number after spinal cord injury^{10,18}. We assessed the location and numbers of astrocytes and microglia after spinal cord injury in 3D, using transgenic mice that express GFP in microglia, *TgH(CX3CR1-EGFP)* mice¹⁹, or in astrocytes, *TgN(hGFAP-EGFP)* mice²⁰. As expected, microglia were evenly spaced in the naive spinal cord (**Fig. 5**). Their density was 70% greater in the gray matter than in the white matter ($6,154 \pm 379 \text{ cells mm}^{-3}$ and $3,565 \pm 194 \text{ cells mm}^{-3}$, respectively; mean \pm s.e.m.; $n = 8$ mice per group), (**Fig. 5a,c,e,h** and **Supplementary Video 10**). Quantifying microglia in conventional tissue sections yielded similar results ($4,991 \pm 264 \text{ cells mm}^{-3}$ in gray and $3,947 \pm 91 \text{ cells mm}^{-3}$ in white matter), but these measurements were more time consuming. We generated an algorithm to automatically identify and count cells and found differences of less than 10% compared to manual counting. For example, the total number of cells in **Figure 5a** is 14,244 when counted manually and 15,350 when counted in a fully automated fashion, an 8% difference (**Supplementary Fig. 12**). Ten days after unilateral dorsal column hemisection, microglia density at the lesion site increased 40-fold in lesioned white matter (**Fig. 5b,d,f,h**, $138,330 \pm 15,105 \text{ cells mm}^{-3}$) and ninefold in lesioned gray matter (**Fig. 5b,d,g,h**, $57,319 \pm 8,037 \text{ cells mm}^{-3}$), as determined by 3D quantification. Microglia density on the contralesion side also increased, but to a smaller extent, about fourfold in both white and gray matter

Figure 3 Visualization of regenerating axons in the unsectioned spinal cord. Regeneration of conditioned axons in GFP-M mice imaged by ultramicroscopy 10 d after injury and subsequent clearing. (**a,b**) 3D reconstruction in sagittal views; **b** shows a higher magnification of the green boxed region in **a**, indicating several regenerating axons (white arrows) crossing the lesion site (yellow rectangle). The distal parts of the injured axons were fragmented and mostly removed by Wallerian degeneration, providing an unambiguous view of regenerating axons beyond the lesion (asterisks). (**c**) 3D reconstruction with a corner-cut view of the spinal cord. The start and end of each traced axon are marked by correspondingly colored arrows and arrowheads, referring to the same axons in all images. (**d**) The tips of the traced axons are shown in xy and xz projections. (**e**) Length of conditioned regenerating axons crossing the lesion site (green dots, $n = 6$ mice) versus stalled unconditioned axons (red dots, $n = 7$ mice) at 10 d after injury. Negative values represent the degeneration distance from the lesion. Positive values represent the length of regenerating axons from the lesion in rostral direction. Each dot represents average values from one mouse. Mean and s.e.m. of each group are indicated by black lines. $**P < 0.01$, t test. (**f,g**) The trajectories of regenerating axons in the white and gray matter of segmented spinal cord in horizontal (**f**) and cross (**g**) views. The yellow and blue marked axons regenerate within the white matter, whereas the red marked axon regenerates through the gray matter.

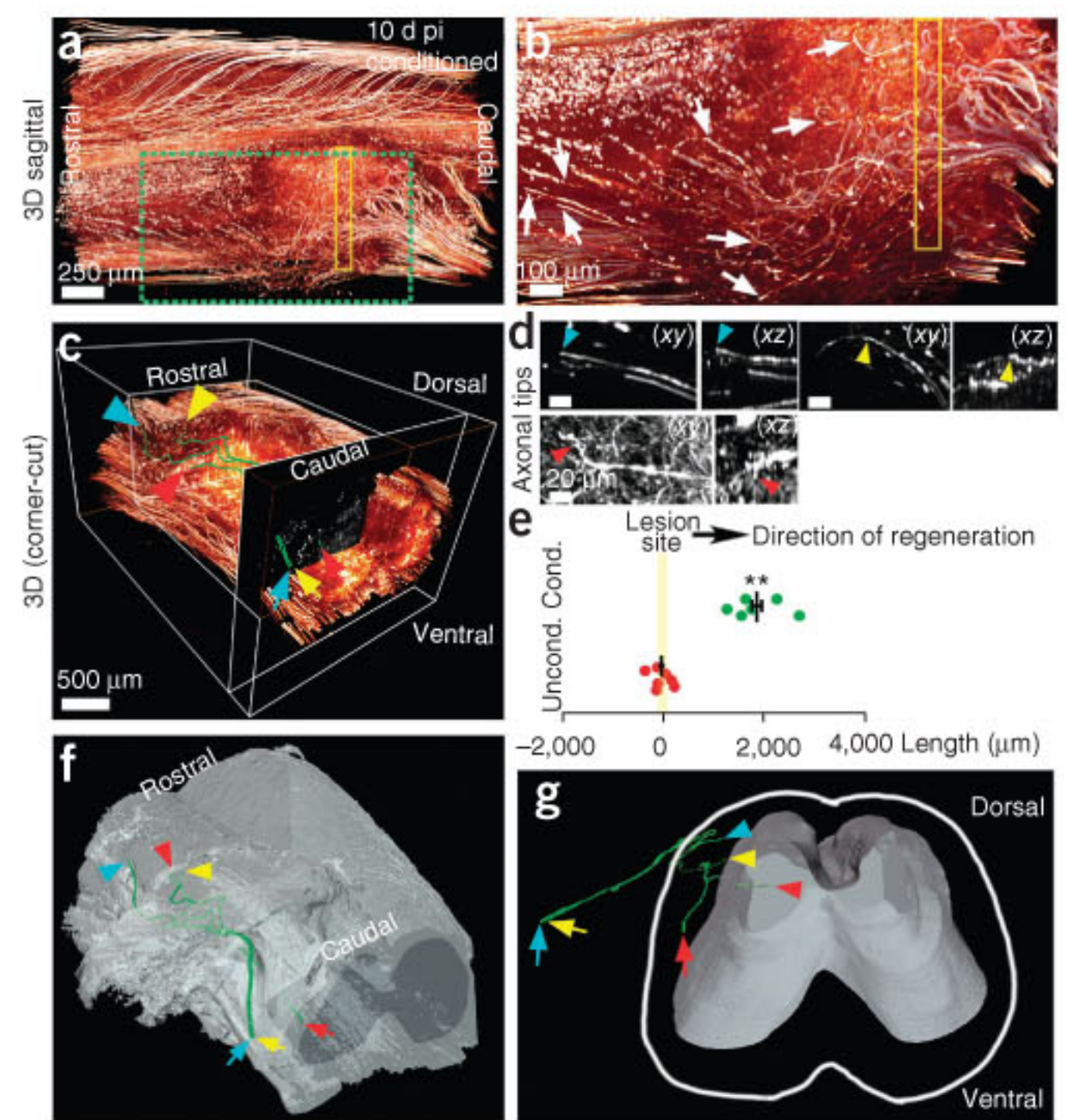


(Fig. 5). The density of GFP-labeled astrocytes was also greater in gray matter than in white matter in the uninjured spinal cord (Supplementary Fig. 13a–e, $26,531 \pm 2,842$ cells mm^{-3} and $8,042 \pm 1,190$ cells mm^{-3} , respectively; Supplementary Videos 11 and 12). In contrast to microglia, astrocytes were only moderately increased

in number after spinal cord injury, twofold and fourfold in injured gray matter and white matter, respectively (Supplementary Fig. 13f–i, $50,788 \pm 4,392$ cells mm^{-3} , $30,128 \pm 408$ cells mm^{-3} , respectively; mean \pm s.e.m.; $n = 6$ mice per group). Thus, 3D visualization of the unsectioned spinal cord allows rapid and precise cell counting.

As the clearing procedure preserved the signal from the different fluorescent proteins equally well, we visualized microglia and neurons after spinal cord injury in double-transgenic mice (expressing GFP and YFP in microglia and neurons, respectively; heterozygous *TgH(CX3CR1-EGFP) × TgN(Thy1-EYFP)* mice; Supplementary Fig. 14 and Supplementary Video 13). We could readily separate overlapping YFP and GFP spectra using spectral imaging and linear unmixing²¹ (described in the Online Methods). Analyzing these mice 10 d after injury showed that lesioned axons retracted and were excluded from the lesion site (Supplementary Fig. 14). In contrast, microglia had

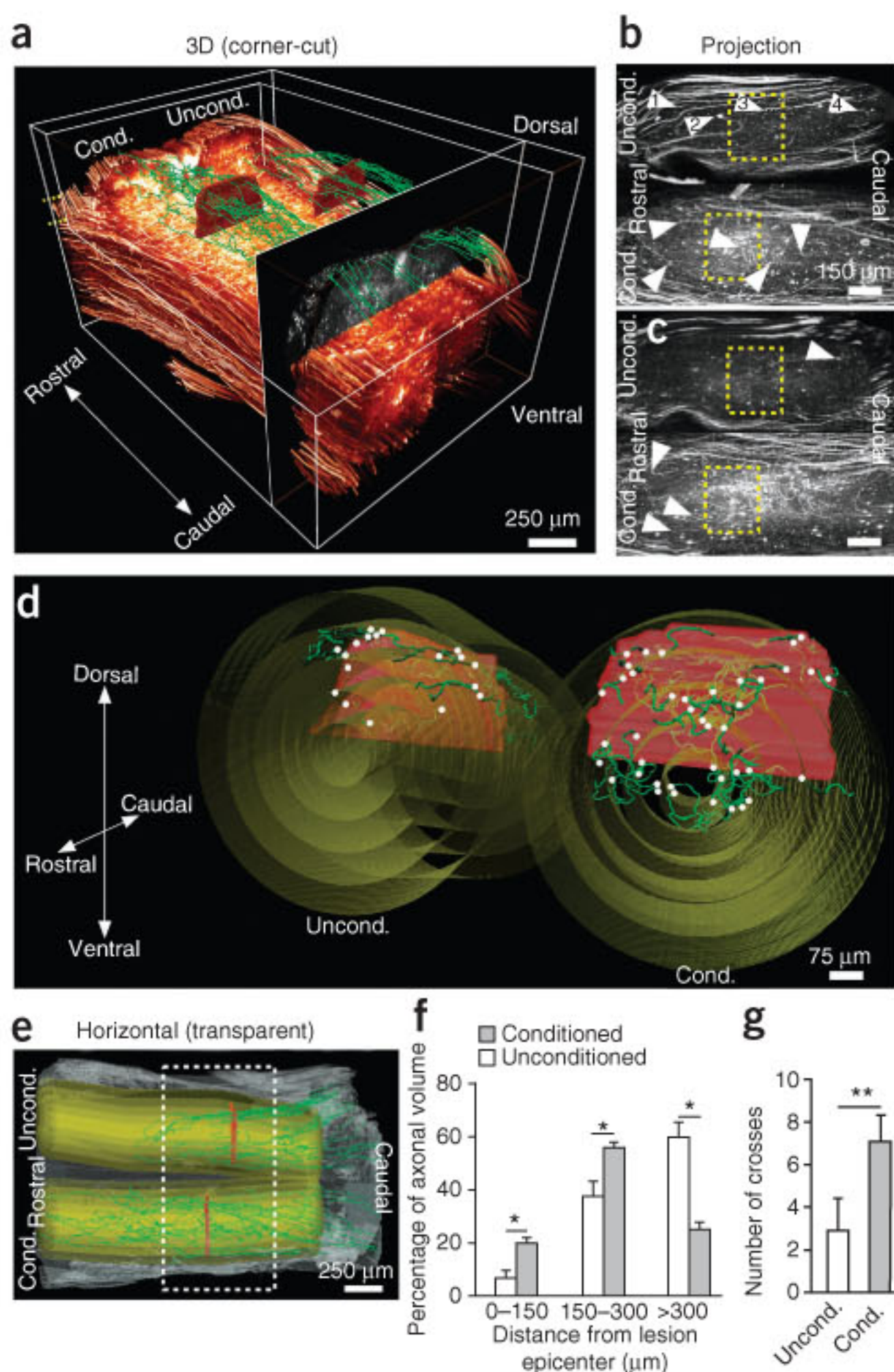
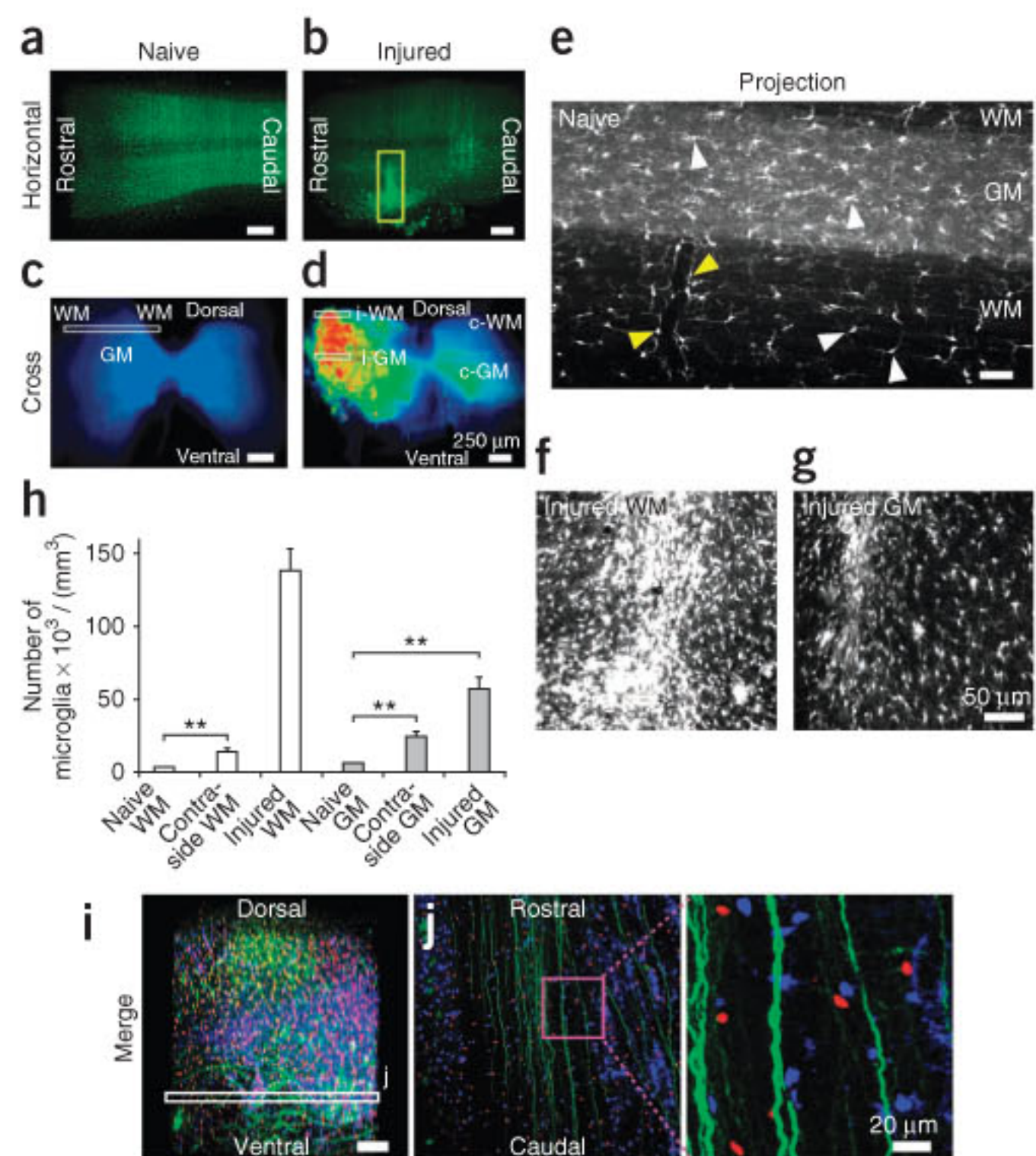


Figure 4 Conditioned axons grow through the lesion, whereas unconditioned axons avoid the lesion. Regeneration of conditioned and unconditioned axons in the cleared GFP-M mouse spinal cord imaged by ultramicroscopy 15 months after injury. (**a**) 3D reconstruction of the trajectories of conditioned versus unconditioned axons (green) in corner-cut view through the lesion (red). (**b,c**) Projections from the indicated regions in **a**. The high magnifications of the axon tips marked with numbered arrowheads in **b** are shown in Supplementary Figure 11. Conditioned axons regenerate over long distances in both dorsal (**b**) and deeper (**c**) layers of the spinal cord (arrowheads). Some unconditioned axons regenerate over short distances and grow on the surface of the dorsal column (**b**) but fewer in deeper regions (**c**) (arrowheads). The yellow dashed rectangles in **b,c** indicate the lesion area. (**d**) Virtual segmentation of the spinal cord into nested cylindrical regions for a 3D Sholl analysis (radius increases in 75-μm increments). White dots mark positions of growing axons at the lesion plane. Conditioned axons were observed in every region of the lesion, and unconditioned regenerating axons were at the edge of the lesion. (**e**) Horizontal transparent view of the spinal cord, depicting the trajectories of stalled or regenerated axons (green). (**f**) The percentage of the axonal volume in the conditioned versus unconditioned ($n = 4$ mice for each) along the indicated cylinder regions (mean \pm s.e.m.). (**g**) The average crossing number of individual axons through cylindrical regions (mean \pm s.d.). $*P < 0.05$, $**P < 0.01$, t test.

Figure 5 Microglia reaction in the injured spinal cord and simultaneous 3D visualization of neurons, astrocytes and microglia. (a,b) 3D visualization of cleared naive (a) and injured (b) spinal cords from *TgH(CX3CR1-EGFP)* mice in horizontal views. (c,d) Spatial distributions of microglia density in the naive (c) and injured (d) spinal cords in cross-sections using color code (blue: low cell density; red: high cell density). The yellow rectangle in b indicates the lesion site. (e) Optical projection of the naive section indicated in c, showing microglia in the gray and white matter (white arrowheads) and adjacent to blood vessels (yellow arrowheads), which appear as black tubes. (f,g) Optical projections from the injured white matter (WM, f) and gray matter (GM, g) regions indicated in d. (h) Quantification of microglia number in the regions depicted in c and d. The values are mean \pm s.e.m.; $n = 8$ *TgH(CX3CR1-EGFP)* mice per group. $^{**}P < 0.01$, t test between groups. Contra, contralateral. (i,j) 3D imaging of neurons, astrocytes and microglia within the same sample using triple-transgenic mice: *TgN(hGFAP-EGFP) \times TgH(CX3CR1-EGFP) \times TgN(Thy1-EYFP)*. (i) 3D visualization of an L1 spinal cord segment from a triple-transgenic mouse showing astrocytes (blue), microglia (red) and neurons (green) in cross-view. (j) Projection (about 50- μ m thickness) of the indicated region in i in horizontal view; higher magnification of the boxed region.



heavily invaded the injury site (Supplementary Fig. 14). In addition, we imaged triple-transgenic mice to simultaneously visualize astrocytes, microglia and neurons (expressing CFP, GFP and YFP in astrocytes, microglia and neurons, respectively; *TgH(CX3CR1-EGFP) \times TgN(Thy1-EYFP) \times TgN(hGFAP-EGFP)* mice; Fig. 5i,j), indicating that various cell types labeled with GFP variants can be imaged in the same tissue after clearing. Thus, clearing allows spatial analysis of glia and axons in the same histologically unsectioned spinal cord.

DISCUSSION

We have established a procedure that allows 3D visualization of cells within unsectioned organs, in particular the adult spinal cord. The technique resulted from a screen of compounds that rendered the tissue transparent by dehydration and lipid extraction. The resulting agent, THF, is a colorless cyclic ether²². It readily dissolves lipids²³ without affecting the fluorescent signal, unlike other lipid-dissolving agents. Our newly developed THF-based clearing procedure renders tissue transparent in a very short time (within 3 h). The transparent tissue can then be imaged with various scanning systems, including two-photon microscopy. We used this technique in the adult CNS, but the procedure can also be applied to other tissues, including lymph node, spleen, lung, mammary gland and various tumor tissues (data not shown). Combining this technique with ultramicroscopy provides the unique advantage of imaging large tissue samples at high resolution. Applying this approach to chronically injured spinal cord pinpointed axonal trajectories that regenerated into the gray matter, which, hitherto, had not been revealed^{4,6,24}. These unusual trajectories could help axons find new targets for reorganizing their circuits. It is notable that 3D imaging also revealed regrowth of unconditioned axons after chronic injury, highlighting a previously underestimated regenerative potential. Because clearing and subsequent 3D imaging allow the tracing of axons up to their tip, it enables unequivocal identification of regenerative axons versus spared axons⁶.

The clearing procedure preserves the signal of various fluorescent proteins, which allows imaging of multiple cell types in one tissue; we simultaneously visualized astrocytes, microglia and neurons in unsectioned CNS tissue. Moreover, THF-based clearing preserved the fluorescence signal of synthetic tracers (except lipophilic dyes); hence, it can also be employed on wild-type animal models²⁵. The clearing procedure cannot be used in combination with electron microscopy because the necessary lipid extraction step disrupts the ultrastructure

of the cells. THF-based clearing permits the use of antibodies for immunocytochemistry. However, penetration of the antibody deeper into tissue is a limiting factor that requires long incubation times.

3D visualization in cleared tissue allows a resolution similar to histological sections. To achieve submicron resolution for tracing fine details in the spinal cord, including small-diameter, unmyelinated axons, we used two-photon imaging with high-numerical-aperture objectives to reach a resolution of 0.5 μ m, in which the field of view is significantly smaller than with ultramicroscopy (0.5–0.6 mm versus 3–4 mm). The clearing procedure allows, in principle, imaging of tissues larger than 4 mm, but currently available objectives pose limits.

Studying the wiring of the nervous system in health and disease is essential for revealing the neuronal basis underlying complex neuronal and psychiatric disorders. Imaging the cleared spinal cord and brain will facilitate ‘connectomics’ approaches aiming to establish the precise wiring of the nervous system²⁶ and will help to interpret regeneration studies. In fact, the exact cellular targets and connection patterns of most descending axonal tracts in adult rodents, perhaps with the exception of the corticospinal tract, are still poorly understood. 3D visualization of unsectioned tissues will be particularly useful for identifying the localization and morphology of cells in single-cell-labeled transgenic mice²⁷ or for describing neuronal circuits traced via *trans*-synaptic viral vector expression²⁸.

In conclusion, we have established a 3D imaging method to identify, trace and evaluate regenerating axons in the unsectioned spinal cord. We also used this method to quantitatively determine the glial response after injury. This approach will allow the precise monitoring of potential therapeutic interventions designed to promote axonal regeneration. This method is relevant not only to spinal cord injury but also to any pathology that affects axons, including neurodegenerative diseases. As the clearing procedure is easy and fast to perform on various tissues and can be combined with different optical imaging techniques, it represents a versatile technique for a broad range of preclinical applications.

METHODS

Methods and any associated references are available in the online version of the paper at <http://www.nature.com/naturemedicine/>.

Note: Supplementary information is available on the Nature Medicine website.

ACKNOWLEDGMENTS

We thank K. Dornmair, J. Enes, C. Hojer, A. Kania, D. Neukirchen, K. Olsen, M. Stuess and S. Tahirovic for critically reading the manuscript, V. Duc Ha for technical assistance and R. Brand for his help with Amira. We are indebted to A. Borst and M. Sheng for their support and to J. Sanes (Harvard University) for the GFP-M mice. A.E. was supported by the Marie Curie Association (European Union; RTN MRTN-CT-2,003-504,636). C.P.M. was supported by the Hertie Stiftung. N.J. was supported by the Theodor Körner Fonds. F.B. is a recipient of a Career Development Award from the Human Frontier Science Program. This work was supported by the Max Planck Society, the International Foundation for Research in Paraplegia and additional grants from the Deutsche Forschungsgemeinschaft and the Hertie Stiftung.

AUTHOR CONTRIBUTIONS

A.E. initiated the project, designed the experiments, developed and performed the clearing protocol, performed the surgeries, performed the *in vivo* confocal and two-photon imaging, analyzed the data, made the figures and videos, performed the statistical tests, and wrote the paper. C.P.M. developed and performed the clearing protocol and performed ultramicroscopy imaging. F.H. performed surgeries and analysis for two-dimensional glia quantification and performed the rat tracing. F.F. developed the automated segmentation, tracking software and analyzed the 3D Sholl data. T.K. and M.H. performed initial two-photon experiments. M.R. and E.K. performed the deep-tissue antibody staining. H.S. and E.K. performed two-photon imaging on double- and triple-transgenic mice. K.B. and N.J. performed the histochemical screen and developed the clearing protocol. H.U.D. constructed ultramicroscopy and supervised C.P.M. F.B. initiated the project, designed experiments, coordinated and supervised the project and wrote the paper. All authors edited the paper.

COMPETING FINANCIAL INTERESTS

The authors declare no competing financial interests.

Published online at <http://www.nature.com/naturemedicine/>.

Reprints and permissions information is available online at <http://www.nature.com/reprints/index.html>.

1. Chen, M.S. *et al.* Nogo-A is a myelin-associated neurite outgrowth inhibitor and an antigen for monoclonal antibody IN-1. *Nature* **403**, 434–439 (2000).
2. Bradbury, E.J. *et al.* Chondroitinase ABC promotes functional recovery after spinal cord injury. *Nature* **416**, 636–640 (2002).
3. GrandPré, T., Li, S. & Strittmatter, S.M. Nogo-66 receptor antagonist peptide promotes axonal regeneration. *Nature* **417**, 547–551 (2002).
4. Neumann, S. & Woolf, C.J. Regeneration of dorsal column fibers into and beyond the lesion site following adult spinal cord injury. *Neuron* **23**, 83–91 (1999).
5. Ramer, M.S., Priestley, J.V. & McMahon, S.B. Functional regeneration of sensory axons into the adult spinal cord. *Nature* **403**, 312–316 (2000).

6. Steward, O., Zheng, B. & Tessier-Lavigne, M. False resurrections: distinguishing regenerated from spared axons in the injured central nervous system. *J. Comp. Neurol.* **459**, 1–8 (2003).
7. Silver, J. & Miller, J.H. Regeneration beyond the glial scar. *Nat. Rev. Neurosci.* **5**, 146–156 (2004).
8. Labombarda, F. *et al.* Modulation of NADPH-diaphorase and glial fibrillary acidic protein by progesterone in astrocytes from normal and injured rat spinal cord. *J. Steroid Biochem. Mol. Biol.* **73**, 159–169 (2000).
9. Wang, L. *et al.* Glial and axonal responses in areas of Wallerian degeneration of the corticospinal and dorsal ascending tracts after spinal cord dorsal funiculotomy. *Neuropathology* **29**, 230–241 (2009).
10. Stuart, D.A. & Oorschot, D.E. Embedding, sectioning, immunocytochemical and stereological methods that optimise research on the lesioned adult rat spinal cord. *J. Neurosci. Methods* **61**, 5–14 (1995).
11. Ylera, B. *et al.* Chronically CNS-injured adult sensory neurons gain regenerative competence upon a lesion of their peripheral axon. *Curr. Biol.* **19**, 930–936 (2009).
12. Kerschensteiner, M., Schwab, M.E., Lichtman, J.W. & Misgeld, T. *In vivo* imaging of axonal degeneration and regeneration in the injured spinal cord. *Nat. Med.* **11**, 572–577 (2005).
13. Enes, J. *et al.* Electrical activity suppresses axon growth through Ca_v1.2 channels in adult primary sensory neurons. *Curr. Biol.* **20**, 1154–1164 (2010).
14. Spalteholz, W. *Über das Durchsichtigmachen von menschlichen und tierischen Präparaten* (S. Hierzel, Leipzig, Germany, 1914).
15. Dodt, H.U. *et al.* Ultramicroscopy: three-dimensional visualization of neuronal networks in the whole mouse brain. *Nat. Methods* **4**, 331–336 (2007).
16. Feng, G. *et al.* Imaging neuronal subsets in transgenic mice expressing multiple spectral variants of GFP. *Neuron* **28**, 41–51 (2000).
17. Ertürk, A., Hellal, F., Enes, J. & Bradke, F. Disorganized microtubules underlie the formation of retraction bulbs and the failure of axonal regeneration. *J. Neurosci.* **27**, 9169–9180 (2007).
18. Faulkner, J.R. *et al.* Reactive astrocytes protect tissue and preserve function after spinal cord injury. *J. Neurosci.* **24**, 2143–2155 (2004).
19. Jung, S. *et al.* Analysis of fractalkine receptor CX(3)CR1 function by targeted deletion and green fluorescent protein reporter gene insertion. *Mol. Cell. Biol.* **20**, 4106–4114 (2000).
20. Nolte, C. *et al.* GFAP promoter-controlled EGFP-expressing transgenic mice: a tool to visualize astrocytes and astrogliosis in living brain tissue. *Glia* **33**, 72–86 (2001).
21. Neher, R. & Neher, E. Optimizing imaging parameters for the separation of multiple labels in a fluorescence image. *J. Microsc.* **213**, 46–62 (2004).
22. Donald Starr, R.M.H. Tetrahydrofuran. *Org. Synth.* **2**, 566 (1943).
23. Díaz, R.S., Monreal, J., Regueiro, P. & Lucas, M. Preparation of a protein-free total brain white matter lipid fraction: characterization of liposomes. *J. Neurosci. Res.* **31**, 136–145 (1992).
24. Freund, P. *et al.* Nogo-A-specific antibody treatment enhances sprouting and functional recovery after cervical lesion in adult primates. *Nat. Med.* **12**, 790–792 (2006).
25. Fouad, K., Klusman, I. & Schwab, M.E. Regenerating corticospinal fibers in the Marmoset (*Callitrix jacchus*) after spinal cord lesion and treatment with the anti-Nogo-A antibody IN-1. *Eur. J. Neurosci.* **20**, 2479–2482 (2004).
26. Lichtman, J.W. & Sanes, J.R. Ome sweet ome: what can the genome tell us about the connectome? *Curr. Opin. Neurobiol.* **18**, 346–353 (2008).
27. Zong, H., Espinosa, J.S., Su, H.H., Muzumdar, M.D. & Luo, L. Mosaic analysis with double markers in mice. *Cell* **121**, 479–492 (2005).
28. Callaway, E.M. Transneuronal circuit tracing with neurotropic viruses. *Curr. Opin. Neurobiol.* **18**, 617–623 (2008).

ONLINE METHODS

Surgical procedures. All mouse experiments were performed in accordance with the animal handling laws of the German government (Regierung von Oberbayern). Mouse surgeries were performed as described¹⁷. We used the following transgenic mice in this study: GFP-M line expressing GFP in neurons¹⁶; *TgH(CX3CR1-EGFP)* line expressing GFP in microglia¹⁹; and *TgN(hGFAP-EGFP)* line expressing GFP in astrocytes²⁰; for the double-transgenic line expressing GFP and YFP in microglia and neurons, respectively, we crossed *TgH(CX3CR1-EGFP)* and *TgN(Thy1-EYFP)*^{19,29} lines; for the triple-transgenic line expressing CFP, GFP and YFP in astrocytes, microglia and neurons, respectively, we crossed *TgN(hGFAP-EGFP)*, *TgH(CX3CR1-EGFP)* and *TgN(Thy1-EYFP)*^{19,29} lines (2–18 months of age; 15–35 g). Whereas all microglia are labeled in *TgH(CX3CR1-EGFP)* transgenic mice, only a subpopulation of neurons (5–10% in GFP-M line) or astrocytes (about 50%) are labeled in *Thy1-GFP* and *TgN(hGFAP-EGFP/GFP)* transgenic mice, respectively.

Perfusion and tissue preparation. Mice were perfused transcardially with 0.1 M phosphate buffer (pH 7.4) for 5–10 min followed by 4% paraformaldehyde (pH 7.4) in 0.1 M PB for 40 min at 3 ml min⁻¹. The dissected spinal cords were post-fixed in 4% paraformaldehyde overnight at 4 °C. On the following day, the dura mater was removed, and the spinal cord was cut into 3- to 4-mm-long segments for the clearing procedure.

Clearing. Samples were incubated in 50% THF (Sigma-Aldrich) for 30 min, in 80% THF for 30 min, three times in 100% THF for 30 min each, in 100% dichloromethane (Sigma-Aldrich) for 20 min and finally in a mixture of benzyl alcohol (Sigma-Aldrich) and benzyl benzoate (Sigma-Aldrich) at a ratio of 1:2 (BABB) for 10 to 15 min, until the samples became transparent.

In thicker tissues (for example, brainstem), we modified the protocol as follows: the tissue was incubated in 50% THF for 1 h, in 80% THF for 1 h, two times in 100% THF for 1 h each, in 100% dichloromethane for 1 h 45 min, and finally in BABB. During all incubation steps, the vial with the sample was kept on a turning wheel in the dark. For confocal and two-photon imaging, we mounted the tissues on a glass slide with a coverslip in BABB. The specimen was immediately imaged by ultramicroscopy or two-photon microscopy. As described for other clearing methods¹⁵, the tissue size anisotropically reduced by 21% in each dimension and 51% in 3D volume.

Two-photon microscopy. Two-photon imaging was performed using a commercial multiphoton laser scanning microscope (Olympus FV1000 Scan unit) with a mode-locked Ti:sapphire laser (Mai Tai, Spectra-Physics) at 910 nm for GFP and 850 nm for simultaneous imaging of GFP, TRITC and A594. We used 20× (0.95 numerical aperture, Olympus) or 25× (1.05 numerical aperture, Olympus) water immersion objectives.

Ultramicroscopy. We used the ultramicroscopy setup as described¹⁵. In short, the specimen was illuminated from the side by a thin sheet of laser light formed by one or two cylinder lenses. Thereby, fluorescence is exclusively generated within the focal plane of the objective, providing a large region of in-focus fluorescence. To combine a large field of view with a reasonable lateral resolution we used a 5× Fluotar (Zeiss) objective with a 0.25 numerical aperture. Several (500–1,000) optical sections were imaged. The scan speed was 0.5–1.5 s per section, which was about 10–30 min for a complete 3D scan.

3D Sholl analysis. The axons of conditioned and unconditioned sides of the spinal cord were traced using filament editor in Amira. The tracing data was imported to MATLAB, where all further analysis was performed. To quantify the distribution of the axons with respect to the lesion epicenter and the spatial curviness of the axons, traced axons were intersected with virtual 3D cylindrical regions of 75-μm ascending radius centered at the site of lesion, parallel to the main axis of the axon bundle. The distribution of the axons in different regions was calculated by quantifying the volume of the axonal structures within each cylindrical region. To quantify the trajectory alterations (spatial curviness) of the individual axons, the intersections of each traced axon with cylindrical regions were counted, and the mean intersection rate was calculated. Conditioned and unconditioned preparations were treated separately.

Image processing and statistical analysis. The individual images and videos were prepared using the 3D image processing software Amira (Visage Imaging). Images were cropped, resized (if necessary) and their brightness adjusted evenly (if necessary) with Photoshop (Adobe) and assembled to figures using Canvas (ACD Systems). Volumes, regions of interest and number of cells were calculated in Amira. We developed algorithms using ImageJ (US National Institutes of Health) and MATLAB to automate tracking, segmentation and counting³⁰ (described in detail in the **Supplementary Methods**). Statistical analysis was performed with Excel (Microsoft), and statistical significance ($P < 0.05$) was calculated using a two-tailed, unpaired Student's *t* test.

Additional methods. Detailed methodology is described in the **Supplementary Methods**.

29. Wang, Y., Zhang, J., Mori, S. & Nathans, J. Axonal growth and guidance defects in Frizzled3 knock-out mice: a comparison of diffusion tensor magnetic resonance imaging, neurofilament staining, and genetically directed cell labeling. *J. Neurosci.* **26**, 355–364 (2006).
30. Cuntz, H., Forstner, F., Borst, A. & Hausser, M. One rule to grow them all: a general theory of neuronal branching and its practical application. *PLoS Comput. Biol.* **6**, e1000877 (2010).